ADVANCED FUNCTIONAL MATERIALS
www.afm-journal.de

3D Printing of Cell-Laden Microgel-Based Biphasic Bioink with Heterogeneous Microenvironment for Biomedical Applications

Yongcong Fang, Yihan Guo, Mengke Ji, Binhan Li, Yujiang Guo, Jieming Zhu, Ting Zhang, and Zhuo Xiong**

A major challenge in 3D extrusion bioprinting is the limited number of bioink that fulfills the opposing requirements for printability with requisite rheological properties and for functionality with desirable microenvironment. Here, this limitation is addressed by developing a generalizable strategy for formulating a cell-laden microgel-based biphasic (MB) bioink. The MB bioink comprises two components, that is, microgels in close-packed condition providing excellent rheological properties for extrusion bioprinting, and a hydrogel precursor that forms a second polymer network to integrate the microgels together, providing post-printing structural stability. This strategy enables the effective printing of a range of hydrogels into complex structures with high shape fidelity. The MB bioink offers great mechanical tunability without compromising printability, and hyperelasticity with superb cyclic compression and stretch endurance. Moreover, the microgels and hydrogel precursor of the MB bioink can encapsulate different types of cells, together creating a heterogeneous cellular microenvironment at microscale. It is successfully demonstrated that hepatocytes and endothelial cells with spatial cell patterning by using MB bioink induce the cellular reorganization and vascularization, leading to enhanced hepatic functions. The proposed MB bioink expands the palette of available bioinks and opens numerous opportunities for the biomedical applications such as tissue engineering and soft robotics.

1. Introduction

3D bioprinting has attracted great interest for its capability to precisely deposit cells and materials (i.e., bioinks) into 3D complex structures, toward applications in engineering in vitro living systems that can be used in disease modeling[1] and tissue regeneration.[2,3] Various bioprinting techniques have been developed so far such as inkjet bioprinting[4] and digital light processing (DLP) -based bioprinting.[5] Among them, the most common modality is extrusion bioprinting, in which a bioink needs to be extruded and then rapidly stabilized to preserve fidelity of the printed structures by digital design.[6] Therefore, the bioinks for extrusion bioprinting are often hydrogels with appropriate rheological properties (i.e., viscosity, shear-thinning, and yield stress) toward printability, which have greatly limited material options.[7] Moreover, there has existed a narrow biofabrication window for bioinks as they need to meet the opposing requirements for printability with high shape fidelity and for functionality with desirable microenvironment.[8] For example, bioinks with higher concentration and thus higher viscosity are preferred for filament extrusion and structural stability, resulting a high shape fidelity,[9] while bioinks with low concentration and thus lower-density polymer networks are beneficial to support cell spreading, migration, and proliferation.[10] Additionally, scaffold-free bioprinting technique provides an alternative strategy to fabricate complex tissue constructs by employing living cell-only aggregations (e.g., spheroids and tissue strands) as building blocks, removing any biomaterial barrier for functional tissue formation.[11] This strategy relies on the inherent ability of cell aggregations to fuse and form larger constructs.[12] Though with high initial cell density and intercellular connection, this approach often fails to maintain the structural stability before tissue fusion due to the inferior mechanical properties of these cell-only building blocks.[13]

In recent years, numerous approaches have emerged to address these challenges.[14] For instance, the addition of

Y. Fang, Y. Guo, M. Ji, B. Li, Y. Guo, J. Zhu, T. Zhang, Z. Xiong
Biomanufacturing Center
Department of Mechanical Engineering
Tsinghua University
Beijing 100084, P. R. China
E-mail: xiongzhuo@tsinghua.edu.cn

Y. Fang, Y. Guo, M. Ji, B. Li, Y. Guo, J. Zhu, T. Zhang, Z. Xiong
Biomanufacturing and Rapid Forming Technology
Key Laboratory of Beijing
Beijing 100084, P. R. China
E-mail: t-zhang@mail.tsinghua.edu.cn

Y. Fang, Y. Guo, M. Ji, B. Li, Y. Guo, J. Zhu, T. Zhang, Z. Xiong
"Biomanufacturing and Engineering Living Systems"
Innovation International Talents Base (111 Base)
Beijing 100084, P. R. China

The ORCID identification number(s) for the author(s) of this article can be found under https://doi.org/10.1002/adfm.202109810.

DOI: 10.1002/adfm.202109810

rheological modifiers such as nanoclays[15] and Pluronic F-127[16] can aid the printability of the hydrogel bioinks with low initial viscosity; however, these additives may have detrimental effects on the cell bioactivities and are usually difficult to degrade.[17] Alternatively, Ouyang et al. expanded the printing capability by incorporating thermo-reversible cytocompatible gelatin, which provides excellent extrusion and structural stability, and can be removed by heating after covalent crosslinking.[18] However, this approach is largely limited to a range of photocrosslinkable bioinks and the removal of gelatin by diffusion usually takes days.[19] The emergence of embedded bioprinting provides a promising approach to address this issue by printing in suspension bath, which provides temporary support for the soft hydrogel bioinks.[20,21] However, the fabrication of suspension bath requires complicated steps or its incomplete removal may have negative effect on printed structures.[22] Another strategy pioneered by Burdick et al. is called jammed microgel (JM) bioink, in which microgels were jammed into inks with remarkable shear-thinning and self-healing properties;[23,24] however, the JM bioink printed structures often lack long-term mechanical stability as they rely solely on physical interactions between microgels, such as electrostatic interaction and hydrogen bonding.[25]

To address these challenges for extrusion bioprinting, here we propose a broadly applicable strategy to formulate a cell-laden microgel-based biphasic (MB) bioink that enables the 3D printing of a range of hydrogels at different polymer concentrations. This MB bioink comprises two components, that is, microgels occupying the major space as discrete phase, and a hydrogel precursor forming a second polymer network as continuous phase to integrate the microgels together. The cross-linked microgel networks provide excellent rheological properties for extrusion during 3D printing, while the hydrogel precursor allows the printed structures to achieve structural stability by post-printing crosslinking. We find that our MB bioink exhibited hyperelastic behaviors and greater cyclic performance than conventional bulk hydrogel and JM bioink. Moreover, the hydrogel precursor could also be incorporated with other types of cells to form heterogeneous cellular microenvironment within a single printed fiber, which was further demonstrated by the example of vascularized hepatic tissues in this work. This generalizable and powerful strategy for designing MB bioink with heterogeneous microenvironment can be further readily applied to other tissue engineering and related biomedical applications.

2. Results and Discussion

2.1. Fabrication and 3D Printing of MB Bioink

Compared to conventional hydrogel bioink, the proposed MB bioink consists of two components: (i) cell-laden microgels in close-packed condition as discrete phase, forming the first network of the MB bioink; (ii) a hydrogel precursor infiltrated into the void spaces as continuous phase, forming a second polymer network between the microgels (**Figure 1**a). To demonstrate the printability of the MB bioink, we used gelatin methacryloyl (GelMA) as representative hydrogel for the MB bioink. 5.0 wt% GelMA was chosen since it represents the minimal polymer concentration that allows for extrusion bioprinting. To illustrate the distribution of the two components of the MB bioink, red and green fluorescein conjugated GelMA were synthesized and used for the microgel networks and hydrogel networks, respectively. We preferred the fluorescent labeled GelMA hydrogels as they eliminate the diffusional effect brought by the physical mixing or electrostatic adsorption methods. The GelMA MB bioink exhibited excellent extrusion and structural stability during 3D printing (Figure 1b). The red fluorescent GelMA microgels with average diameters of 175 μm occupied around 80% volume of MB bioink, while green fluorescent GelMA hydrogel filled into the interspaces between microgels as expected (Figure 1c).

The fabrication of MB bioink is illustrated in Figure 1d, where we use the flow-focusing microfluidic devices to generate microgels. Cell-laden hydrogel precursor were injected into the microchannel and sheared by the continuous oil flow to form droplets, which were further stabilized during cross-linking. To replace the void space between microgels with another hydrogel precursor, microgels were centrifugated to remove extra fluids and further supplemented with hydrogel precursor solution. The process repeated several times when the concentration of hydrogel precursor surrounding microgels reached its original values. We encapsulated C2C12 myoblast cells within 5.0 wt% GelMA microgels as an example. We found that the optimal light intensity for simultaneous targeting for high cell viability and microgel stability was around 80 mW cm^{-2} with an exposure time of 35 s (Figure S1, Supporting Information). The viability of C2C12s within microgels was around 91.5% ± 4.2% as shown by live/dead staining (Figure 1e).

We further used Brdu staining to label the proliferating cells within microgels (Figure 1f). The proliferation rate increased as high as 69.8% ± 8.5% with prolonged culture times (Figure 1g). C2C12 migrated and spread at the outer surfaces of microgels as indicated by F-actin staining (Figure 1h). There is much versatility to this approach provided by the microfluidic devices, allowing the fabrication of cell-laden microgels from a broad variety of materials and across a wide range of sizes and cellular density. We successfully generated varied sizes of microgels with cellular density up to 50 million per mL, which is difficult to achieve with conventional extrusion bioprinting (Figure 1i). It is noteworthy that the fabrication of cell-laden microgels is also applicable to other current spheroid or droplet formation techniques such as microfluidic devices,[26] ultra-low attachment plates,[27] bioprinting,[28] and magnetic levitation,[29] which suggests the huge potential of MB bioink in regenerative medicine applications.

We printed MB bioink encapsulated with C2C12s as a proof of concept (Figure 1j). The sizes of microgels and printed fibers were 203.5 ± 14.8 μm and 535 ± 35.2 μm, respectively, indicating that there were up to six microgels at the cross-section area of printed fibers (Figure 1k). The microgel compaction condition can be adjusted by changing the centrifugation force, which has an impact on the viability of encapsulated cell as well (Figure S2, Supporting Information). Here, we used centrifugation force at 270 G and 500 G to generate MB bioink, of which the cell viabilities were 80.3% ± 3.6% and 73.3% ± 3.4%, respectively; however, the cell viability of previously reported JM bioink generated by vacuum filtration approach was only 36.4% ± 3.3%, equivalent to the one (33.5% ± 8.6%) at much

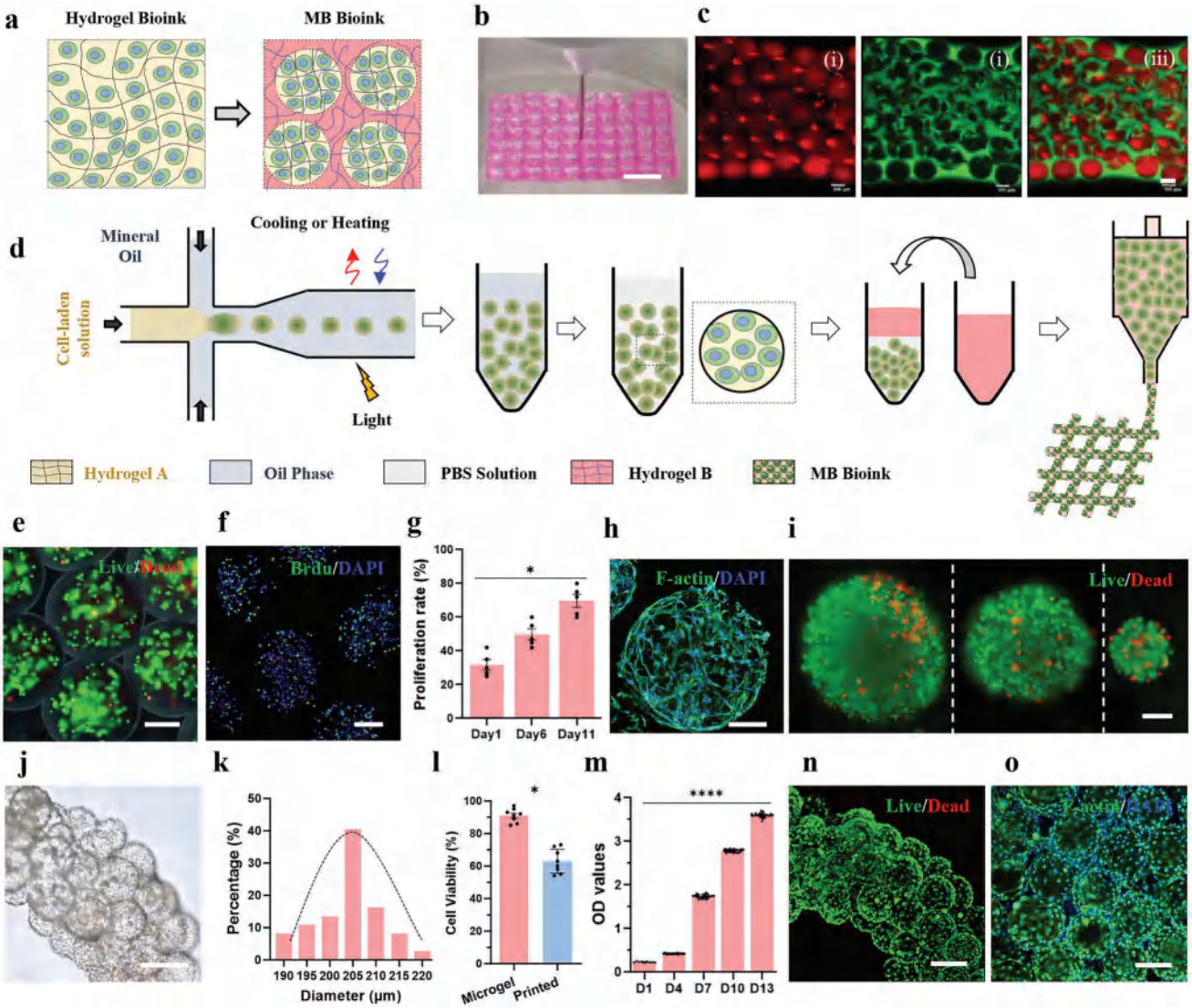

Figure 1. Fabrication and 3D printing of cell laden MB bioink. a) Schematic representation of hydrogel bioink and MB bioink. b) 3D printing mesh-like structures with MB bioink. c) MB bioink consisting of microgels (5.0 wt% GelMA, marked with red fluorescence) as discrete phase and second polymer network (5.0 wt% GelMA, marked with green fluorescence) as continuous phase. d) Step-by-step illustration of the fabrication process of MB bioink. e) Calcein-AM/PI staining showing high viability of C2C12s-laden microgels. f) Brdu staining labeling proliferating cells with microgels. g) Proliferation rate of cells within microgels with prolonged culture time. h) F-actin staining showing cytoskeletal of C2C12s-laden microgels. i) Varied sizes of microgels at close to physiological cellular density (50 millions per mL). j) 3D printed fibers with cell-laden microgels-based bioink at day 7. k) Size distribution of microgels within fibers. l) Cell viability before and after printing. m) Proliferation rates of cells within MB bioink printed fibers. n) Calcein-AM/PI staining showing high cell viability of microgels-based fibers. o) F-actin staining showing cytoskeletal of microgels-based fibers. Scale bars in (b): 5 mm, (c): 100 μm, (e,f): 200 μm, (h,i): 100 μm, (j,n,o): 200 μm. One-way ANOVA was used to analyze the data, $*p < 0.05$, $****p < 0.0001$.

higher centrifugation force of 4000 G. Therefore, the reported extraction-supplement approach provides a simple and gentle way to incorporate living cells into MB bioink. After printing and photo-crosslinking, the cell viability within microgels decreased to 62.8% ± 7.4%, indicating that shear forces during printing and post-printing light irradiation impacted cell viability as well (Figure 1l). The phenomenon of cell damage during extrusion printing and photo-crosslinking was also observed for pure GelMA hydrogel ink, with cell viability decreasing from 97.0% ± 1.3% to 84.4% ± 3.8% (Figure S3, Supporting Information).

Despite their relatively lower initial viability after printing, C2C12s encapsulated in the printed fibers exhibited high growth rate with prolonged culture times (Figure 1m). The cell viability within printed fibers on day 7 was observed to exceed 95% as C2C12 proliferated (Figure 1n, Figure S4, Supporting Information). C2C12s migrated to outer surfaces of microgels and further infiltrated into the void spaces between microgels as shown by F-actin and smooth muscle alpha-actin (αSMA) staining for longer culture time (e.g., ≈10–14 days) (Figure 1o, Figure S5, Supporting Information). Moreover, the GelMA microgels quickly swelled after transferring to aqueous phase from oil phase (Figure S6a, Supporting Information), and the swelling ratio of MB bioink printed structure was around 13.3 ± 0.66 (Figure S6b, Supporting Information), suggesting

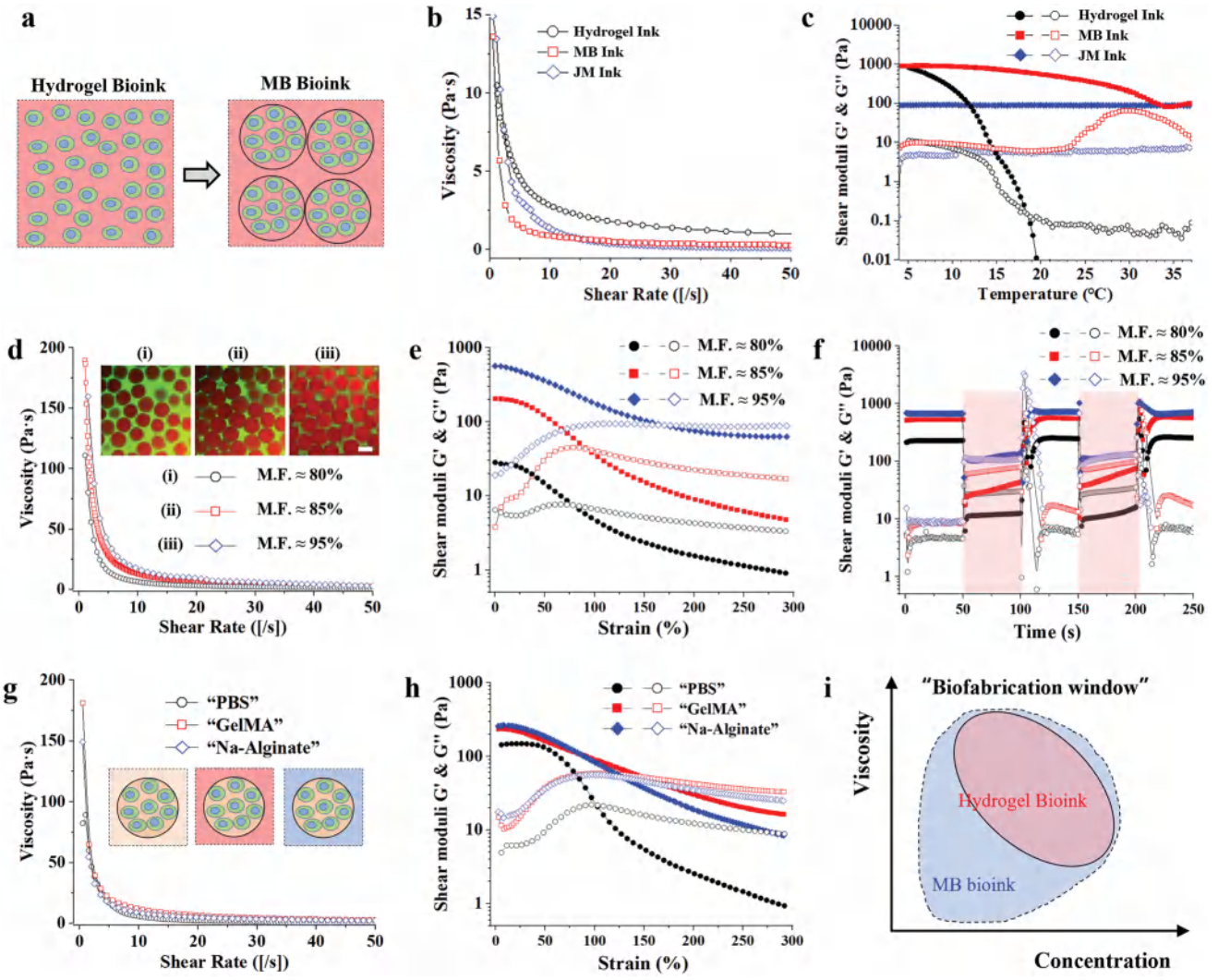

Figure 2. Rheological characterization and diversity in compositions of MB bioink. a) Schematic representation of pure hydrogel bioink and MB bioink. b) Rheological characterization of pure hydrogel, MB ink, and JM ink (all with 5.0 wt% GelMA) all showing decreased viscosity with continuously increasing shear rates (0–50 s^{-1}). c) Rheological characterization showing shear moduli of MB ink and JM ink are independent of temperature, while GelMA hydrogel has critical gel-sol phase transition point. Rheological characterization of MB bioink with microgel fractions at 80%, 85%, and 95% showing d) shear-thinning properties, e) strain yielding with increase in strain (0–300%, 1 Hz), and f) self-healing through low (unshaded, 1% stain, 1 Hz) and high (shaded, 300% stain, 1 Hz) strain cycles. Inset in (d): fluorescent images showing varied compaction conditions with microgel fraction (MF) at i) 80%, ii) 85%, and iii) 95% (scale bars: 200 µm). Rheological characterization of MB bioink with different continuous phase including PBS solution, GelMA precursor solution and sodium alginate solution showing g) shear-thinning and h) strain yielding properties. i) Design of MB bioink expanding 3D bioprinting capability with extended biofabrication window.

that MB bioink was suitable for tissue engineering application. It is noteworthy that the swelling ratio of MB bioink was smaller than its GelMA hydrogel counterpart (17.2 ± 0.5), probably due to the higher crosslinking degree of microgels. Collectively, the fabrication strategy of MB bioink is highly amiable to the encapsulated cells and could be further extended to other types of cells for tissue regeneration.

2.2. Rheological Properties of MB Bioink

Rheological properties of bioink are essential for extrusion bioprinting.[11] Here we compared the rheological properties of MB bioink with bulk hydrogel and JM bioink using 5.0 wt% GelMA as representative hydrogel (**Figure 2**a). Microgels and hydrogel precursor of MB bioink had the same composition as GelMA hydrogel to avoid any unwanted interferences caused by the heterogeneity in the material composition. JM bioink completely made of 5.0 wt% GelMA microgels were generated by vacuum filtration approach as previously reported.[23] As expected, 5% GelMA hydrogels, the JM, and MB bioink all displayed shear-thinning behavior, that is, decreased viscosities with increasing shear rate at room temperature (Figure 2b). Generally, GelMA hydrogels possess the inherent temperature-dependent sol-gel transition of gelatin, originating from the triple helix formation of denatured collagen fibers.[30] For

5.0 wt% GelMA hydrogel bioink, the sol-gel transition temperature is around 18.5 °C. However, the MB bioink maintained in the gelled state (storage modulus (G′) > loss modulus (G″)) across the temperature range of ≈4–35 °C, while the shear moduli of JM bioink were completely temperature independent as these GelMA microgels were highly crosslinked (Figure 2c). Compared to conventional GelMA hydrogel inks, the temperature independent nature of the MB bioink indicated the extended biofabrication window for 3D bioprinting applications.

The rheological properties of MB bioink are highly regulated by the microgel fraction (MF) of the bioink. We prepared MB bioink by mixing red fluorescent GelMA microgels with green fluorescent GelMA precursor solution for visualization. The microgel fraction of MB bioink was measured by the 3D reconstruction of z-stacks obtained from the laser confocal micro_scopy of the printed fibers (Movie S1, Supporting Information). By controlling the centrifugation force, the microgel fraction can be tuned. Here, we compared three conditions of MB bioink with MF at ≈80%, ≈85%, and ≈95%. MB bioink with MF less than 80%, which possessed rather low viscosity for extrusion bioprinting, was not included for comparison. Although all three groups of MB bioink exhibited shear-thinning properties, increasing the microgel fraction increased the viscosity of MB bioink (Figure 2d). The MB bioink behaved like an elastic hydrogel at low strains (G′ > G″), but then yield at higher strains (G″ > G′) (Figure 2e). The yield strain (where G′ = G″) of MB bioink increased as the microgel fraction increased, indicating higher strain was needed to disrupt contacts between microgels when at a more closely packed condition. Moreover, all three groups of MB bioink exhibited self-recovery properties. In other words, the MB bioink underwent a rapid, reversible transition from a solid-like, elastic state (G′ > G″) at low strain (1%) to a liquid-like viscous state (G″ > G′) at high strain (300%) in oscillatory strain sweeps (Figure 2f). It is noted that this self-recovery behavior is temperature independent as the phenomenon was observed at temperatures varying between ≈4 and 37 °C (Figure S7, Supporting Information).

To test whether our MB bioink is compatible with various crosslinking strategies of the second networks, we used sodium alginate and GelMA as the hydrogel precursor of the MB bioink, respectively. After printing, sodium alginate was crosslinked with calcium ions and GelMA precursor was crosslinked by exposure to visible light (405nm), allowing the printed structures to achieve the mechanical robustness. The shear-thinning (Figure 2g) and yield stress (Figure 2h) properties were observed for the MB bioink with varied second networks, even with phosphate-buffed saline (PBS) as second phase. Therefore, the rheological properties that are required for extrusion bioprinting rely on the closely packing condition of microgels and are independent of the compositions of microgels and second network. It is noteworthy that mechanical forces can easily disrupt the printed structures when using PBS filling the void space of microgels, indicating the second network to chemically integrate microgels together by post-crosslinking is essential for the structural stability and mechanical properties of 3D printed structures.

Further, we fabricated MB bioink with microgels made of GelMA at much lower concentration and other biopolymers such as sodium alginate, respectively. We successfully generated 3.75 wt% GelMA microgels at the optimal light intensity and exposure time of 40 mW cm^{-2} and 45 s, respectively. These low-concentration GelMA microgels maintained long-time stability in PBS solution, with cell viability up to 67.5% ± 9.1% (Figure S8a, Supporting Information). Further, GelMA MB bioink with microgels at lower concentration (3.75 wt%) exhibited similar shear-thinning behavior (Figure S8b, Supporting Information) and strain yielding (Figure S8c, Supporting Information) properties. We generated 0.5 wt% alginate microgels using microfluidic device, supplemented with ion crosslinking. After collection, the cell viability of alginate microgels was around 85.3% ± 6.4% (Figure S8d, Supporting Information). The Alg/GelMA MB bioink prepared by mixing alginate microgels with GelMA precursor also exhibited shear-thinning behavior (Figure S8e, Supporting Information) and strain yielding properties (Figure S8f, Supporting Information), suggesting that their capability to be used for extrusion bioprinting. Taken together, the generalizable strategy for the MB bioink greatly expanded the extrusion printing window to meet the biological needs of printed tissues as they enable the printing of those low concentration and low viscosity hydrogels in the modality of microgels (Figure 2i).

2.3. Printability of MB Bioink

To illustrate the printability of the MB bioink, a vertical filament was extruded through a 510 μm inner diameter nozzle (21 gauge) on suspension. The filament was extended smoothly for 3 cm long until it collapsed by gravity, with diameter close to that of the nozzle (**Figure 3**a(i)). Meanwhile, we fabricated JM bioink to compare its printability with our MB bioink (Figure S9a,b, Supporting Information). For JM bioink, the excess water in the interstitial spaces was extruded first, and microgels were packed closer before yielding to flow as previously reported.[23,24] We observed a clogging problem and the discontinuous extrusion of JM bioink during printing (Figure S9c, Supporting Information), which was consistent with previous report;[31] whereas, for MB bioink, microgels (red fluorescent) were evenly extruded with interstitial hydrogel precursor (green fluorescent) due to less resistance (Figure 3a(ii) and Movie S1, Supporting Information). Further, we optimized the 3D printing parameters including the printing speed at 1 mm s^{-1} and extrusion rate at 0.35 μL s^{-1} before printing complex structures (Figure S10, Supporting Information). A multi-layered mesh of 15.0 × 25.0 mm^2 with filament spacing of ≈1.75 mm was printed and further stabilized by post-crosslinking with a 405nm light (Figure 3b(i)). The junctions of two perpendicular filaments in the 3D meshes displayed good interconnectivity between adjacent layers as characterized under microscopy (Figure 3b(ii)). We printed a double-ring structure with rhodamine-conjugated GelMA MB bioink to visualize the granular morphology of the printed fibers (Figure 3c). It should be noted that the nozzle temperature during printing could be extended from 15 to 30 °C without affecting printing fidelity owing to its temperature-independent rheological properties of MB bioink. This consistency is highly advantageous, particularly for multi material 3D printing and bioprinting in extreme environmental conditions with temperature instability.

We printed standard tubular structures to quantitatively evaluate the shape fidelity by using MB bioink (Figure 3d).

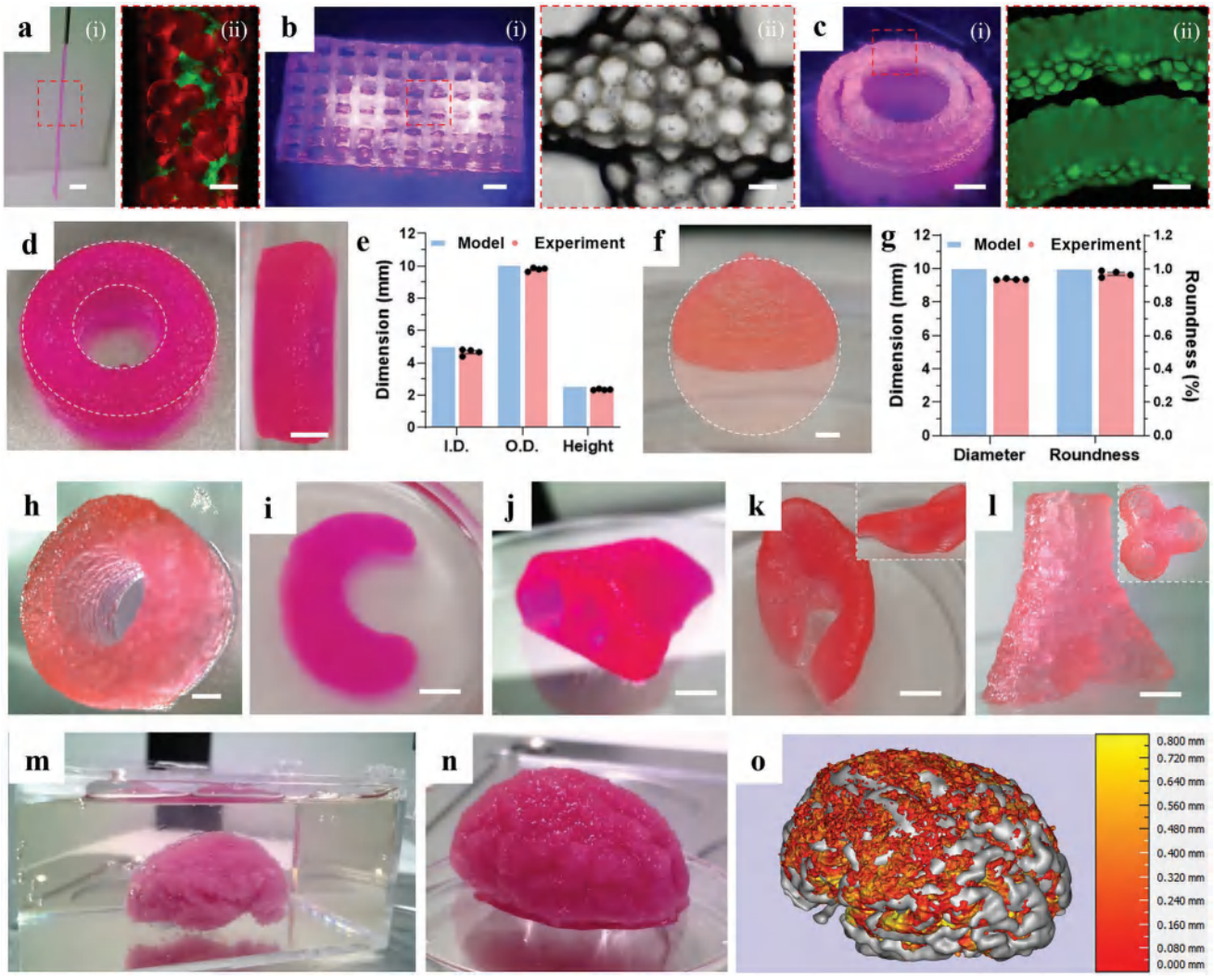

Figure 3. 3D printing capability and fidelity using MB bioink. a-i) Filament extrusion of MB bioink and ii) magnified view under confocal microscopy, with microgels (5.0 wt% GelMA) marked with red fluorescence and second hydrogel (5.0 wt% GelMA) marked with green fluorescence. b) 3D printed mesh-like structures i) using MB bioink, with magnified view ii) at the intersection. c) 3D printed double rings i) crosslinked upon visible light (405 nm) exposure, with rhodamine conjugated GelMA microgels ii) under confocal microscopy. d) 3D printed tubular structures (left, top view; right, side view). e) Measured inner diameter (ID), outer diameters (OD), and height of 3D printed ring structures in (d). f) 3D printed hemisphere using MB bioink. g) Measured diameter and roundness. h) 3D printed large vessel, i) meniscus, j) nose, k) ear, and l) bronchus. Inset in (k) represents the oblique view and inset in (l) represents the vertical view. m) Suspension printing of brain model using MB bioink. n) A photograph of a printed brain model after removing from the suspension bath. o) A heat map showing the geometric difference between the template (gray color) and the print (red and orange color). Scale bars in (a,b): 2 mm in (i) and 200 µm in (ii), (c): 2 mm in (i) and 500 µm in (ii), (d,f): 2 mm, (h–l): 5 mm, (o): 5 mm.

After crosslinking, the inner diameter (ID), outer diameter (OD), and height of printed structures were measured. They were slightly lower than the input values, with the marginal reduction (less than 5%) attributed to the width of the filament building blocks (Figure 3e). Owing to the inherently layer-by-layer deposition fashion, it is usually challenging for conventional 3D bioprinting to achieve smooth curves in the vertical direction. Here, we printed hemispheres (diameter: 10 mm) by using the GelMA hydrogel bioink, MB bioink, and JM bioink, respectively (Figure S11a, Supporting Information). The printed hemisphere was projected on the glass surface into a complete sphere, of which the diameter and roundness were measured by Image J software (Figure S11b,c, Supporting Information). The hemisphere printed by MB bioink exhibited a smoother interlayer transition (Figure 3f), with closer to the input values (e.g., diameter, and roundness), suggesting a higher structural fidelity imparted by the MB bioink (Figure 3g).

We explore the 3D bioprinting of human anatomical structures using MB bioink for potential biomedical applications such as tissue engineering.[32] We printed thick vessels (Figure 3h), menisci (Figure 3i), noses (Figure 3j), ears (Figure 3k), and bronchi (Figure 3l) as representative examples as they encompass challenging geometrical features (e.g., overhangs, thin walls, and branches), which is rather challenging for conventional extrusion bioprinting with soft hydrogels. The bronchus model contains 50 layers, with a height of 15 mm, an

interior diameter of 5 mm, and a wall of 1 mm thickness. Surprisingly, the freshly printed bronchus with such a high aspect ratio and thin wall excellently supported their own gravity during printing and resulted in a high structural fidelity of MB bioink. Moreover, we successfully printed a brain model by utilizing suspension printing strategy (Figure 3m). The bioprinted brain model showed typical folded and wrinkled area on the surface (Figure 3n). Volumetric 3D digital reconstructions of the bioprinted brain mimic were compared with the volumetric 3D digital template using Magics software. A distance map from the overlaid template and printed structures was generated (Figure 3o), and the fraction of voxels of the printed structure within 0.5 mm of the template was found to be around 94.6%, showing a high level of printing fidelity of MB bioink. In all cases, we observed excellent extrusion consistency and structural stability through the 3D printing process. Moreover, the 3D-printed models maintained their geometries and dimensions over a week when placed in culture medium.

2.4. Hyperelastic Behaviors of MB Bioink

The mechanical properties of the printed structures play a pivotal role in biomedical applications including tissue regeneration,[33] hydrogel machines,[34] and soft robotics.[35] To compare their mechanical properties, we printed cylinders (diameter:10 mm, height: 5 mm) as samples with GelMA hydrogel bioink, MB bioink, and JM bioink with the same polymer concentration, respectively (**Figure 4**a). The MB bioink and JM bioink exhibited greater elasticity than GelMA bulk hydrogel probably owing to the displacement of microgels, as evidenced by their significantly lower elastic modulus (MB bioink: 2.7 ± 0.3 kPa; JM bioink: 2.2 ± 0.2 kPa) than GelMA bulk hydrogel (15.4 ± 1.0 kPa) (Figure 4b). Moreover, for MB bioink, microgels were further confined within the second networks under compression, resulting in a relatively higher elastic modulus compared to JM bioink.

More importantly, we explore the cyclic compression endurance of MB bioink as many soft tissues (e.g., cartilages) and natural materials are subjected to complex loading profiles such as cyclic compression.[36] For GelMA hydrogel bioink, fatigue crack growth was soon initiated within the printed cylinders after several compression cycles at only 40% strain (Movie S2, Supporting Information). Similarly, for JM bioink, the printed cylinders quickly fatigued after less than 20 compression cycles at 60% strain, with the maximum-stress loss up to 50% (Figure 4c; Movie S3, Supporting Information). However, for MB bioink, the printed cylinders can be repeatedly

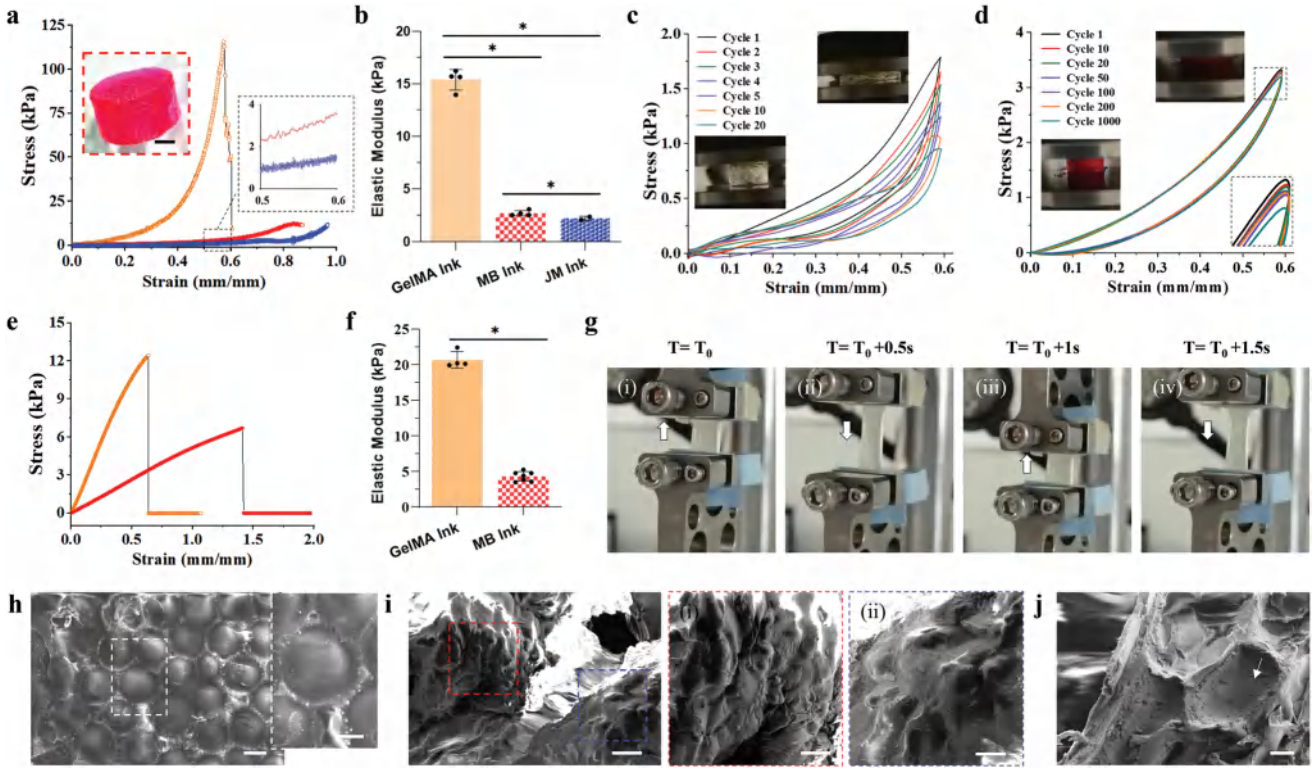

Figure 4. Mechanical characterization of MB bioink printed constructs. a) Representative stress–strain curves and b) compressive elastic moduli of printed cylinders using 5 wt% GelMA hydrogel, MB ink, and JM ink, respectively. c) The cyclic endurance test of printed cylinders using JM ink at 60% strain for 20 compression cycles. d) The cyclic endurance test of printed cylinders using MB ink at 60% strain for 1000 compression cycles. Insets: images of GelMA cylinders at $\varepsilon = 0\%$ (bottom) and 60% strain (top). e) Representative stress–strain curves and f) elastic moduli of printed strips at uniaxial tension using 5 wt% GelMA hydrogel and MB ink. g) Digital images of 3D printed strips using MB ink under 100% strain and release. h–j) The SEM images showing the morphology of the MB ink printed structures h) before and i,j) after cracking. Insets: magnified images demonstrating the intact structure of microgels at the cracking area. Scale bars in (a): 2 mm, (h): 100 µm (inset: 50 µm), (i): 100 µm (inset (i,ii): 50 µm), (j): 20 µm. Student's *t*-test was used to analyze the data, $^*p < 0.05$.

compressed at 60% strain for 1000 times (Movie S4, Supporting Information). All the hysteresis loops of MB bioink group overlapped very well, and all the unloading curves returned to the original points (Figure 4d), indicating its hyperelastic behavior that nearly no plastic deformation occurred under such intensive loading for thousands of times.

We printed 3D strips to examine the mechanical properties under uniaxial stretch and cyclic stretch performance of MB bioink. MB bioink exhibited much higher fracture strain (141.7% ± 5.2%) than GelMA hydrogels (63.8% ± 3.1%) (Figure 4e), and much smaller elastic modulus (4.3 ± 0.7 kPa) than GelMA hydrogels under stretch (20.7 ± 1.2 kPa) (Figure 4f), which was consistent with the results at compression (Figure 4b). Moreover, the printed strips using JM bioink were mechanically weak such that they can easily collapse under stretch and thus not included for comparison, suggesting the addition of a second network to covalently integrate the microgels together is essential for our MB bioink. The printed strips using MB bioink can be stretched by extreme deformation of up to 100% strain and recover to its original shape upon relaxation (Figure 4g; Movie S5, Supporting Information). Scanning electron microscopy (SEM) images of freeze-dried structures corroborated the characteristic granularity of the MB bioink (Figure 4h). Moreover, most of the microgels at the cracking area appeared to remain intact (Figure 4i) or completely detached from the second polymer network (Figure 4j), suggesting the potential mechanism of energy dissipation by displacement of microgels. Collectively, these data demonstrated the extraordinary structure robustness and cyclic performance of our MB bioink, which may advance the in vitro engineering of certain natural tissues such as cartilages[37] and ligaments,[38] and is desirable for other biomedical applications such as soft robotics[39] and artificial muscles.[40]

Moreover, the mechanical properties of our MB bioink can be easily tuned by adjusting the stiffness of the microgels and second hydrogel phase without sacrificing any of its printability. For instance, the stiffness of GelMA microgels could be easily tuned by adjusting the light intensity and exposure time (Figure S12a,b, Supporting Information). The MB printed cylinders consisting of stiffer microgels (elastic modulus at 65.3 ± 11.6 kPa) appeared to be stiffer (elastic modulus at 9.4 ± 1.1 kPa) than the ones (elastic modulus at 4.7 ± 0.7 kPa) with softer microgels (elastic modulus at 30.1 ± 8.6 kPa) mainly due to the less deformation of microgels under compression (Figure S12c,d, Supporting Information). Similarly, the MB bioink with 5.0 wt% GelMA (2.7 ± 0.3 kPa) as the second network were stiffer and tougher than the ones with 2.5 wt% GelMA (2.2 ± 0.1 kPa) and 1.5 wt% sodium alginate (Na-Alg) (1.7 ± 0.2 kPa) as the second network, respectively (Figure S13a,b, Supporting Information). Interestingly, the MB bioink formed with lower concentration (2.5 wt%) of GelMA and sodium alginate as second network also exhibited hyperelastic behavior, without fatigue crack growth after 1000 compression cycles at 60% strain (Figure S13c,d, Supporting Information). It should be noted that the addition of cells to the MB ink increased the compressive modulus whether the cells were encapsulated into microgels or second hydrogel phase (Figure S14a,b, Supporting Information) probably due to the particle reinforcement effect of cells within microgels and hydrogel; however, their cyclic performances seemed to be reduced (Figure S14c,d, Supporting Information).

2.5. Heterogeneous Microenvironment of MB Bioink Facilitates Hepatic Function

Most of the human tissues and organs are composed of various cell types that generate heterogeneity in cellular and material compositions at the microscale level.[41] For instance, the human liver is a highly vascularized organ that is mainly made up of hepatic lobules.[42] As a small functional unit of the liver, a hepatic lobule is composed of the hepatocytes, sinusoidal lumen, biliary canaliculi, Disse space, Kupffer cells, and stellate cells within the vascular system. Another notable advantage of our MB bioink lies in the fact that the hydrogel precursor could also be incorporated with other types of cells such as endothelial cells, different from the cells encapsulated in microgels, together creating a heterogeneous cellular microenvironment within a single printed fiber. We hypothesize that the microscale heterogeneous microenvironment of MB bioink induces the vascularization of the printed hepatic tissues, and further facilitates the hepatic function as illustrated in **Figure 5**a.

Here we used two immortalized cell lines, that is, human hepatocarcinoma cell line HepG2 and human umbilical cord endothelial cells (HUVECs) for hepatic study as primary human hepatocytes and endothelial cells are difficult to seek and culture.[43] To test our hypothesis, we encapsulated HepG2 and HUVECs within the microgels and hydrogel precursor of the MB bioink, respectively. As control group, HepG2 and HUVECs were directly mixed at the same cellular density. To eliminate the potential effect caused by varied material composition, we use 7.5 wt% GelMA for both the microgels and hydrogel precursor of the MB bioink, the same as the pure hydrogel bioink. First, we generated HepG2-laden microgels with high cell viability (≈90%) and albumin (ALB) expression as shown in Figure S15a,b, Supporting Information). Moreover, the printed hepatic tissues using MB bioink maintained their structural integrity and high cell viability with prolonged culture (Figure S15c,d, Supporting Information).

By using CellTracker Fluorescent Probes, we successfully marked HepG2 and HUVECs with red and green fluorescent colors, respectively, for better visualization of cellular distribution within both bioinks. The red fluorescent HepG2 cells were uniformly mixed with green fluorescent HUVECs at ratio of 4:1 in the hydrogel bioink group (Figure 5b(i)). However, HUVECs were mainly confined to the inter-microgel region in the MB bioink group (Figure 5c(i)). Notably, HUVECs within MB bioink groups exhibited a much higher proliferation rate with elongated morphology on days 3 and 7 compared to those in pure hydrogel bioink (Figure 5b(ii),c(ii), Figure S16, Supporting Information). We attribute this to the enrichment effect associated with the confinement of endothelial cells in the MB bioink, resulting in locally increased cell density and enhanced cellular interactions for both hepatic and endothelial cells. Subsequently, the printed structures were immunostained with albumin for HepG2 and anti-von willebrand factor (vWF) for HUVECs on day 6. It should be noted that the experiment with cells without fluorescent probing was also performed at the exact same conditions to illuminate any potential effect by the fluorescent cell tracker reagents. For MB bioink, HUVECs spread relatively well and formed random tube-like vascular structures by endothelial cell assembly, covering the

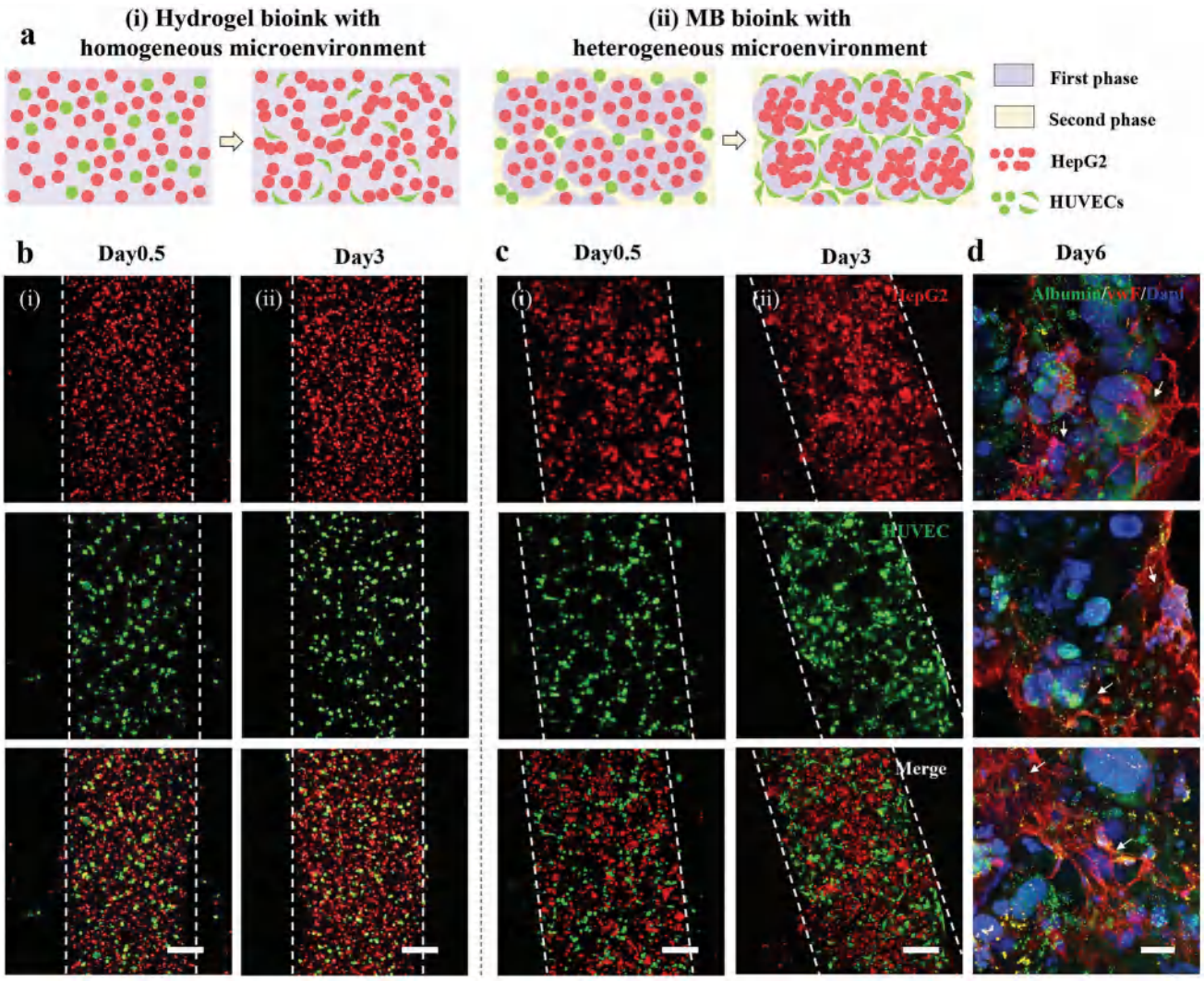

Figure 5. 3D printing vascularized hepatic tissue constructs with tunable heterogeneous microenvironment. a) Schematic illustration of each type of cell, that is, HepG2 (red) and HUVECs (green), with spatial cellular arrangement for hydrogel bioink and MB bioink with 7.5 wt% GelMA. b) HepG2 (red) and HUVECs (green) cells within printed fibers using hydrogel bioink on i) day 1 and ii) day 3, with white dotted lines indicating the boundaries of printed fibers. c) HepG2 (red) and HUVECs (green) cells within printed fibers using MB bioink on i) day 1 and ii) day 3. d) Immunostaining of albumin for HepG2 and vWF for HUVECs on day 6, with white arrows pointing to the vessel formation by EC assembly. Scale bars in (b,c): 200 µm, (d): 50 µm.

surface of HepG2 microgels (Figure 5d). Further, quantitatively analysis of vessel formation demonstrated the greater extent of capillary-like network formation within MB ink over hydrogel ink (Figure S17, Supporting Information). In turn, the printed hepatic tissues exhibited higher proliferation rates (**Figure 6**a) when present with spatial cell arrangement endowed by MB bioink, which enhanced cellular organization of each cell type.

Although the greater extent of structural heterogeneity and cell reorganization found in the printed structures using MB bioink is very encouraging, it is also important to investigate the maturation level based on liver-specific functions and gene expression. Therefore, we first analyzed the anabolic and catabolic functional aspects of human liver by comparing the albumin secretion and urea production from breaking down of amino acids. The 2D culture model was used as a benchmark against which the relative change of albumin and urea in printed hepatic tissues using hydrogel bioink and MB bioink can be measured (Figure 6b,c). The normalized secreted albumin and urea levels by cell numbers in both models were initially lower than that in 2D culture model; however, the trend was reversed on day 7 possibly due to the cell contact inhibition in 2D culture model. Secreted albumin and urea levels in hydrogel bioink group were consistently lower than that in MB bioink group. It should be noted that the albumin and urea levels were gradually increased in hydrogel and MB bioink group on day 7, whereas they decreased in 2D culture model on day 7.

Encouraged by the observed functional enhancement, we proceed to evaluate the expression levels of key enzymes in liver drug metabolism, for example, the cytochrome P450 (CYPs) enzymes in hepatocytes.[44] Specifically, we used two representative CYPs, CYP3A4 and CYP1A1, which account for nearly 60% CYP activity.[45] For instance, CYP3A4 as the largest member of the CYP3A subfamily, is estimated to be responsible for 40% to

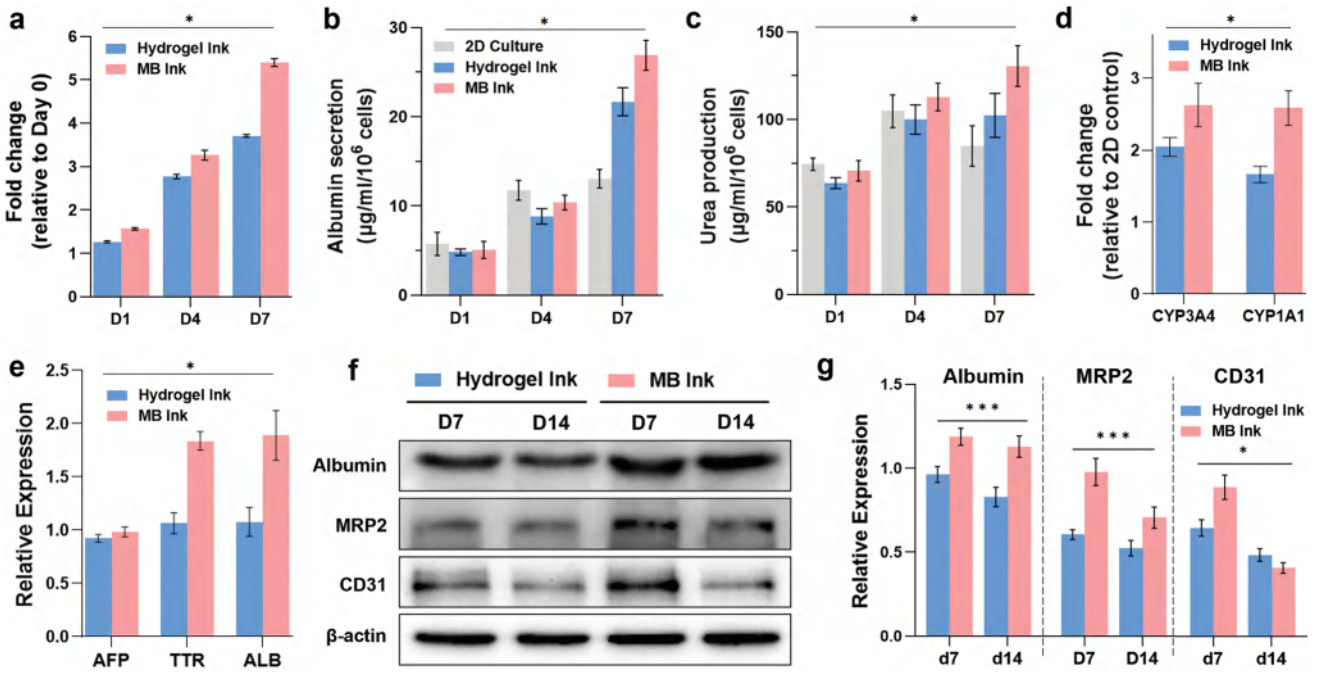

Figure 6. Evaluation of hepatic function and liver-specific gene and protein expression levels. a) Cell proliferation measured by CCK-8 assay. b) Analysis of albumin secretion by ELISA. c) Analysis of urea production by ELISA. d) Analysis of CYP3A4 and CYP1A1 enzyme activity. e) Gene expression profiles comparing the ALB, TTR, and AFP expression levels of the printed hepatic constructs with pure GelMA hydrogel and MB bioink on day 10. f) Western blot analysis of albumin and MRP2 for HepG2 and CD31 for HUVECs on days 7 and 14 following bioprinting. g) Relative protein expression of albumin, MRP2, and CD31. Two-way ANOVA was used to analyze the data, $*p < 0.05$, $***p < 0.001$.

50% of all phase I metabolism.[46] We assessed enzyme activity of CYP3A4 and CYP1A1 without any drug treatment on day 10. For 2D culture of HepG2/HUVECs, P450 enzyme activity was measured at day 7 as these cells could not survive for longer time. The results demonstrated that both enzyme activities of hydrogel bioink and MB bioink groups were much higher than that of 2D culture model. MB bioink group showed higher enzyme activity of CYP3A4 and CYP1A1 compared to hydrogel bioink group (Figure 6d).

Further, we seek to explore the expression levels of liver-specific genes and functional proteins that play a pivotal role in regulating the liver functions. The expression levels of mature hepatic markers, for example, transthyretin (TTR) and ALB, were much higher in MB bioink group compared to hydrogel bioink group, while the expression levels of fetal hepatic marker alpha-fetoprotein (AFP) were not significantly different (Figure 6e). Similarly, western blot analysis showed that overall albumin and multidrug resistance protein 2 (MRP2) protein levels were higher in MB bioink group compared to hydrogel bioink group despite of the fact that the protein levels of albumin and MRP2 were decreased from days 7 to 14 in both groups. In addition, platelet endothelial cell adhesion molecule-1 (PECAM-1, CD31) expression was significantly higher in MB bioink group on day 7 (Figure 6f,g). Therefore, these findings demonstrated a relatively more mature gene and protein expression profile of hepatocytes in MB bioink. Taken together, in this study, we demonstrated that hepatocytes and endothelial cells with spatial cell patterning in MB bioink facilitated cellular reorganization and vascularization, resulting in enhanced hepatic functions and maturation level of liver-specific gene and protein expression. Although advanced 3D bioprinting strategies have been widely leveraged to produce heterogenous tissue constructs;[47] however, they highly rely on modifying the print head system such as coaxial printing,[48] multi-material microfluidic printing,[49] and DLP-based bioprinting integrating with material exchanging system.[50] Alternatively, we present a simple way to print heterogeneous tissues with heterogeneity solely offered by MB bioink, in which varied types of microgels with different encapsulated cells, composition, structure, and mechanical stiffness could be further mixed and assembled. In the future, the MB bioink could be further incorporated with current printing strategies to better mimic the structural complexity and heterogeneity of native tissues and organs.

3. Conclusion

In conclusion, we introduce the concept of cell-laden microgel-based double biphasic (MB) bioink as a generalizable strategy for 3D extrusion bioprinting. The MB bioink is composed of cell-encapsulated microgels that are jammed and connected through a second crosslinked polymer network. This approach offers excellent bioprinting capabilities with extended biofabrication window provided by the rheological properties (i.e., shear-thinning, yield stress, and self-recovery) of the MB bioink. We printed 3D complex structures including noses, ears, bronchus, and brain models with high shape fidelity. Moreover, MB bioink offers great tunability in mechanical properties without sacrificing any of its printability and exhibited hyperelastic behaviors, superb cyclic compression, and stretch endurance. This generalizable and powerful strategy offers a more effective methodological approach to 3D printing heterogeneous

tissue constructs, whereby the MB bioink can be readily tuned to achieve heterogeneous cellular microenvironment at the microscale level. Our demonstration of hepatic tissue printing indicated that locally increased cell density with spatial cell patterning in MB bioink accelerated cellular reorganization and vascularization, and further facilitated the functional maturation of the printed hepatic tissue constructs. Overall, the flexibility in the design of MB bioink with mechanical tunability, hyperelasticity, and heterogeneous microenvironment opens new possibilities for 3D bioprinting in biomedical applications such as tissue engineering and soft robotics.

4. Experimental Section

Materials: GelMA and lithium phenyl-2,4,6-trimethylbenzoylphosphinate (LAP) used in the study were purchased from EFL Inc., China. The degree of methacrylation (defined as the ratio of functionalized to original amino groups) was 60%. Fluorescein-conjugated GelMA and rhodamine-conjugated GelMA were synthesized by reacting GelMA with NHS-Fluorescein (#46409, Thermo Fisher Scientific) and NHS-Rhodamine (#46406, Thermo Fisher Scientific), respectively. Briefly, 1 g GelMA was fully dissolved in 20 mL of phosphate buffer (pH ≈ 8.1) at 37 °C, followed by the addition of 50 mg NHS-Fluorescein or NHS-Rhodamine, and reaction under stirring was conducted at 37 °C in for 24 h the dark. The solution was then dialyzed (MWCO, 5 kDa) at 37 °C for 1 week by changing the deionized water. The dialyzed solution above was freeze-dried for later use.

Cell Culture: C2C12 myoblast cells and HepG2 were purchased from China Infrastructure of Cell Line Resources in Beijing. C2C12s were cultured in Dulbecco's modified eagle's medium (DMEM, Thermo Fisher) in addition to 10% fetal bovine serum (FBS, Bioind), 1% penicillin/streptomycin (100 U mL^{-1}, Life Technologies), and 1% MEM nonessential amino acids (NEAA, Life Technologies). HepG2 cells were cultured in Gibco Minimum Essential Media (MEM, Thermo Fisher) supplemented with 10% FBS and 1% penicillin/streptomycin. HUVECs were purchased from American Type Culture Collection (ATCC, CRL-1730) and cultured with customized culture medium from Lonza (CC3126). All cells were detached from the cell culture dish using 0.25% Trypsin-EDTA (Life Technologies) and then counted using automatic cell counter (Countstar, China) before mixing with prepared bioink for bioprinting. To illustrate the spatial arrangement of cells, HepG2 and HUVECs were marked with red and green fluorescent colors using CellTracker Deep Red dye (C34565, Life Technologies) and Green CMFDA dyes (C2925, Life Technologies).

Microgel Fabrication: Microchannels of T-junction microfluidic device were first primed with mineral oil (sigma) supplemented with 2% span 80 at the flow rate of 75 µL min^{-1}. Cell-laden polymer precursor solution consisting of 5.0 wt% or 7.5 wt% GelMA and 0.25 wt% LAP was heated at around 30 °C, injected at the flow rate of 15 µL min^{-1} and sheared into monodisperse droplets at the merging points of both fluids. The polymer droplets were in situ crosslinked by exposure to visible light at 405 nm (100 mW cm^{-2}, ≈25 s) at the outlet. Microgels were centrifugated at 1200 rpm for 5 min to remove the oil layer on top and rinsed with Dulbecco's phosphate-buffered saline (Gibco) for three times. For fabrication of alginate microgels, a mixture of mineral oil (48 mL), aqueous $CaCl_2$ solution (0.5 g mL^{-1}, 1.0 mL), and Span80 (1.0 mL) was sonicated for 5 min to make the oil emulsion. 0.5 wt% alginate (MQ300, Sigma Aldrich) and oil emulsion were injected into the microfluidic chip to generate droplets at the flow rate of 15 µL min^{-1} and 100 µL min^{-1}. After collection, the oil supernatant was aspirated, and 2.0 wt% $CaCl_2$ solution was added to further gel alginate microgels for 1 min. alginate microgels were rinsed with PBS for three times before use. The diameters and roundness of microgels were analyzed using Image J software (NIH).

MB Ink Preparation: The rinsed microgels in PBS solution were centrifugated at 1200 rpm for 3 min to remove extra fluids. The polymer precursor solution consisting of 5.0 wt% GelMA and 0.25 wt% LAP was then added as second hydrogel phase to mix with microgels. The mixture was centrifugated at 1200 rpm again to remove extra fluids and further supplemented with fresh 5.0 wt% GelMA precursor solution. The process was repeated at least three times until the inter-microgel space was fully replaced by the second hydrogel phase. To visualize the distribution of microgels within the prepared inks, the prepolymer solution of microgels and second hydrogel were conjugated with red and green fluorescent colors.

Bioprinting: 3D bioprinting was performed using a commercial 3D bioprinter (Biomaker 2i, Sunp BioTech). Cell-laden MB inks were loaded into 3 mL syringes (BD) and centrifuged at 1000 rpm for 1 min to remove any bubbles. 3D models including cubes, cylinders, noses, menisci, and ears were converted to STL files and imported to generate gcode readable by the bioprinter. A printing speed of 1 mm s^{-1}, extrusion rate of 0.35 µL s^{-1} and 21-gauge needles were used to print these constructs. After printing, micro computed X-ray tomography (micro-CT) was performed to evaluate the printing fidelity using a desk top µCT machine (Skyscan 1272, Bruker, Belgium) with a 10 µm pixel size. SEM was used to observe the microstructure of MB bioink printed structures. The samples were freeze-dried, and sputter coated with gold (thickness, 10 to 20 nm), and imaged with a Zeiss Auriga SEM system at 10 kV. To print hepatic tissue constructs, 7.5 wt% GelMA microgels containing 7.5×10^6 HepG2 cells per mL mixed with second precursor solution (7.5 wt% GelMA) containing 1.5×10^6 HUVECs per mL were used as MB bioink. 7.5 wt% GelMA precursor solution containing directly mixed HepG2 cells (final concentration: 7.5×10^6 per mL) and HUVECs (final concentration: 1.5×10^6 per mL) were used as conventional bioink as control. Printing temperature for MB bioink and 7.5 wt% GelMA bioink was around 21 °C. After printing, the constructs were crosslinked by exposure to 405 nm light at 40 mW cm^{-2} for 80 s, flipping the constructs carefully half-way through the process.

Cell Viability: Cell-laden microgels and printed structures were performed with cell viability assay by using Calcein-AM/PI Double Staining Kit (C542, Dojindo Molecular Technologies). Briefly, after removing the culture medium, the samples were washed with PBS three times, and incubated with 2 mM Calcein AM (live cell stain, green) and 4.5 mM Propidium Iodide (dead cell stain, red) at 37 °C for 30 min. After the incubation, the samples were visualized using a laser-scanning confocal microscope (FV3000, Olympus), and cell viability was calculated by dividing live cell numbers by total cell numbers.

Brdu Staining: The thymidine analog 5-bromo-2′-deoxyuridine (BrdU) staining was performed to label the proliferating cells according to the manufacture's instruction by using the BrdU Immunohistochemistry Kit (ab125306, Abcam). Briefly, Brdu was added to culture medium at a concentration of 3 µg mL^{-1}. After incubation at 37 °C for 2 h, the microgels were fixed with 4% paraformaldehyde and blocked with 5% normal horse serum (in PBS with 0.1% Triton X-100). Microgels were incubated with anti-Brdu primary antibody overnight, followed by incubation in second antibody (polyclonal anti-rat Alexa Fluor 488, Abcam) for 2 h at room temperature. DAPI was added to the solution in order to label all cell nuclei.

Proliferation Assay: Cell Counting Kit-8 (CCK-8, Dojindo Molecular Technologies) were used to assess cell proliferation within microgels or printed constructs on days 1, 4, 7, and 10. Briefly, samples were transferred to one well of 12-well plates containing 1 mL medium supplemented with 100 µL of CCK-8 solution, and incubated at 37 °C for 2 hr. After incubation, 110 µL of the supernatant was transferred to 96-well plate. This absorbance was measured at 450 nm using a microplate reader (Multiskan FC Microplate photometer, Thermo Scientific). The optical density (OD value) for absorbance was directly proportional to the number of living cells. For each condition, at least three samples were tested.

Rheological Characterization: Rheological properties of conventional bulk hydrogel and MB bioink were measured using a rheometer (MCR301, Anton Paar) with a 25 mm diameter cone plate geometry and gap size of 200 µm. Thermo sensitive behavior of bioink was investigated by measuring the G′ and G″ at varied temperatures from

4 to 37 °C (strain: 1%, frequency:1 Hz). The shear-thinning behavior was investigated by measuring shear viscosity in continuous flow at ramped shear rate from 0 to 50 s^{-1}. Strain sweeps ranging from 0.1% to 300% at 1 Hz frequency were performed to examine dynamic yielding properties. To demonstrate self-recovery properties, the G′ and G″ were measured with alternated low (1%) and high (300%) strains (1 Hz, 50 s) for three cycles.

Atomic Force Microscopy (AFM) Analysis: The surface elastic modulus of microgels was An measured using AFM-assisted nanoindentation as previously described.[51] AFM (MFP-3D-SA, Asylum Research) was used for measurements on a vibration isolation table (Herzan, Laguna Hills). A tipless silicon nitride cantilever (MLCT-O10, Bruker) was located and positioned with a 5 µm polystyrene bead (Bangs Labs, Fishers) over the center of each GelMA microgel under a bright field microscope (Eclipse Ti, Nikon). The polystyrene beads possessed an elastic modulus of 3.5 GPa and poisson's ratio of 0.32. The elastic modulus of each GelMA microgel was determined using IGOR software, where the Hertzian contact model was applied to the extension force–displacement curves.

Mechanical Property: Samples with 10 mm circular diameter and 5 mm height were printed using conventional bulk hydrogel and MB bioinks, respectively. Prior to all measurements, all samples were measured with vernier caliper to determine their actual sizes. Four samples of each condition were loaded and compressed until rupture at the rate of 0.05 mm s^{-1} using a mechanical test instrument (Bose ElectroForce 3200, Bose Corp.). Similarly, tensile measurements were performed by uniaxial stretch test of printed strips (lenght:25 mm, width: 5 mm, thickness: 2.5 mm). The elastic part (10% to 20% strain) of the stress–strain curve was used to calculate the elastic modulus. To determine the hyperelastic behaviors and cyclic performance of MB constructs, samples were repeatedly applied with high-strain compression (strain: 60%) and stretch (strain: 100%) for at least 10 min.

Immunofluorescence Staining: For 3D printed hepatic tissues with HepG2 cells and HUVECs, hydrogel bioink and MB bioink groups were stained with albumin and vWF to verify hepatic function and vasculature, respectively. Briefly, the samples were removed from culture medium and washed with PBS three times. The washed samples were then fixed in 4% formaldehyde solution for half an hour and rinsed with PBS five times. For permeabilization, the samples were soaked with 0.1% Triton-X 100 for 30 min and blocked with 10% goat serum albumin in PBST solution (0.1% Tween in PBS) for 1 h. The samples were incubated with primary antibodies against albumin (1:100, ab10241, Abcam) and vWF (1:200, ab76533, Abcam) at 4 °C overnight. Subsequently, the samples were repeatedly rinsed with PBS to remove unconjugated antibodies, followed by an overnight incubation using Alexa Fluor 488 goat anti-mouse (1:500) for albumin and Alexa Fluor 647 donkey anti-sheep (1:500) for vWF. Finally, the samples were counterstained with 4′,6-diamidino-2-phenylindole (DAPI, blue) and visualized using a laser-scanning confocal microscope (FV3000, Olympus). Likewise, 3D tissue constructs printed with C2C12s-laden microgels were stained with phalloidin (ab176753, Abcam) and smooth muscle alpha-actin (ab5694, Abcam), respectively. The total capillary-like length, the average length of capillary-like network, and the number of capillary-like branches were quantified on 3D projected confocal images by Image J software with the Angiogenesis Analyzer plugin tool.

Albumin Secretion and Urea Synthesis: For evaluating hepatic functions, each group of cell culture supernatants was collected for 1, 4, and 7 days and stored at −20 °C before use. The culture medium was changed every day, and four samples were used for each group and grown in one well of 12-well plate. Albumin secretion was assessed using the human albumin in vitro ELISA (Enzyme-Linked Immunosorbent Assay) kit (SEKH-00081, Solarbio), and urea production was measured using a Urea Assay Kit (ab234052, Abcam) according to the manufacturer's instructions. The amount of albumin and urea secretion was calculated based on the standard curve from each experiment followed by normalization to the cell number using CCK8 assay as beforementioned.

Enzyme Activity: The CYP1A1 and CYP3A4 activity were performed according to the manufacture's instruction by using the P450-Glo CYP1A1 and CYP3A4 assay kit (Promega). 2D culture with HepG2 cells and HUVECs at the same initial cellular density was utilized as a control group. The activity of each enzyme was measured using a GloMax navigator microplate luminometer (Progema).

Western Blotting: Western blotting was performed as described previously.[52] Briefly, protein was isolated in RIPA lysis and extraction buffer with protease inhibitor and phosphatase inhibitor cocktail (Cell Signaling). Protein concentration was determined by BCA assay (Sigma). Protein extracts were separated by sodium dodecyl sulfate polyacrylamide gel electrophoresis and transferred to a polyvinylidene difluoride (PVDF) membrane. Primary antibodies against albumin (500:1, ab10241, Abcam), MRP2 (500:1, ab3373, Abcam) and CD31 (200:1, ab76533, Abcam) were applied overnight at 4 °C overnight. Subsequently, the proteins were detected with Goat anti-Rabbit IgG (H+L) Cross-Adsorbed Secondary Antibody (1500:1, Thermo Fisher Scientific, G-21234) or Goat anti-Mouse IgG (H+L) Cross-Adsorbed Secondary Antibody (1500:1, Thermo Fisher Scientific, G-21040). The protein levels were visualized with the ChemiDoc touch imaging system (Bio-rad) and analyzed using Image J software.

RT-PCR: Total RNA was purified from samples according to the manufacturer's instructions using TRIzol (Thermo Fisher). Reverse transcription was performed using the iScript cDNA Synthesis Kit (Bio-Rad) following the manufacturer's instructions. Gene expression was quantified by real-time PCR using SYBR Green primers (Life Technologies) in an Applied Biosystems Step One Plus. Data analysis was carried out using the fold change normalized to glyceraldehyde-3-phosphate dehydrogenase (GAPDH) gene expression. Primers used are listed in Supporting Information as "Primer list."

Statistical Analysis: Data are expressed as mean ± SEM. Differences between experimental groups were analyzed by student *t*-test, one-way or two-way ANOVA. Post hoc pairwise analysis was done using Tukey's HSD test. P values <0.05 were considered significant for statistical tests.

Supporting Information

Supporting Information is available from the Wiley Online Library or from the author.

Acknowledgements

The authors acknowledge the financial support from the National Key Research and Development Program of China (2018YFA0703004) and China Postdoctoral Science Foundation (2021TQ0184).

Conflict of Interest

The authors declare no conflict of interest.

Data Availability Statement

The data that support the findings of this study are available in the supplementary material of this article.

Keywords

3D printing, bioinks, hyperelastic, microgels, tissue engineering

Received: November 13, 2021
Revised: November 27, 2021
Published online: December 16, 2021

[1] S. Park, D. Zhang, Y. Qi, Y. Li, K. Y. Lee, V. J. Bezzerides, P. Yang, S. Xia, S. L. Kim, X. Liu, F. Lu, F. S. Pasqualini, P. H. Campbell, J. Geva, A. E. Roberts, A. G. Kleber, D. J. Abrams, W. T. Pu, K. K. Parker, *Circulation* **2019**, *140*, 390.
[2] A. C. Daly, M. E. Prendergast, A. J. Hughes, J. A. Burdick, *Cell* **2021**, *184*, 18.
[3] Y. Song, X. Su, K. F. Firouzian, Y. Fang, T. Zhang, W. Sun, *Biofabrication* **2020**, *12*, 035016.
[4] X. Li, B. Liu, B. Pei, J. Chen, D. Zhou, J. Peng, X. Zhang, W. Jia, T. Xu, *Chem. Rev.* **2020**, *120*, 10793.
[5] C. Yu, J. Schimelman, P. Wang, K. L. Miller, X. Ma, S. You, J. Guan, B. Sun, W. Zhu, S. Chen, *Chem. Rev.* **2020**, *120*, 10695.
[6] I. Matai, G. Kaur, A. Seyedsalehi, A. McClinton, C. T. Laurencin, *Biomaterials* **2020**, *226*, 119536.
[7] L. Y. Zhou, J. Fu, Y. He, *Adv. Funct. Mater.* **2020**, *30*, 2000187.
[8] R. Levato, T. Jungst, R. G. Scheuring, T. Blunk, J. Groll, J. Malda, *Adv. Mater.* **2020**, *32*, 1906423.
[9] A. Schwab, R. Levato, M. D. Este, S. Piluso, D. Eglin, J. Malda, *Chem. Rev.* **2020**, *120*, 11028.
[10] L. N. West-Livingston, J. Park, S. J. Lee, A. Atala, J. J. Yoo, *Chem. Rev.* **2020**, *120*, 11056.
[11] V. Mironov, R. P. Visconti, V. Kasyanov, G. Forgacs, C. J. Drake, R. R. Markwald, *Biomaterials* **2009**, *30*, 2164.
[12] N. Khoshnood, A. Zamanian, *Bioprinting* **2020**, *19*, e00088.
[13] A. Ovsianikov, A. Khademhosseini, V. Mironov, *Trends Biotechnol.* **2018**, *36*, 348.
[14] S. V. Murphy, A. Atala, *Nat. Biotechnol.* **2014**, *32*, 773.
[15] Q. Gao, X. Niu, L. Shao, L. Zhou, Z. Lin, A. Sun, J. Fu, Z. Chen, J. Hu, Y. Liu, Y. He, *Biofabrication* **2019**, *11*, 035006.
[16] X. Li, H. Wang, D. Li, S. Long, G. Zhang, Z. Wu, *ACS Appl. Mater. Interfaces* **2018**, *10*, 31198.
[17] S. Hong, D. Sycks, H. F. Chan, S. Lin, G. P. Lopez, F. Guilak, K. W. Leong, X. Zhao, *Adv. Mater.* **2015**, *27*, 4035.
[18] L. Ouyang, J. P. K. Armstrong, Y. Lin, J. P. Wojciechowski, C. Lee-Reeves, D. Hachim, K. Zhou, J. A. Burdick, M. M. Stevens, *Sci. Adv.* **2020**, *6*, c5529.
[19] Y. Zhao, R. Yao, L. Ouyang, H. Ding, T. Zhang, K. Zhang, S. Cheng, W. Sun, *Biofabrication* **2014**, *6*, 035001.
[20] A. Lee, A. R. Hudson, D. J. Shiwarski, J. W. Tashman, T. J. Hinton, S. Yerneni, J. M. Bliley, P. G. Campbell, A. W. Feinberg, *Science* **2019**, *365*, 482.
[21] N. Noor, A. Shapira, R. Edri, I. Gal, L. Wertheim, T. Dvir, *Adv. Sci.* **2019**, *6*, 1900344.
[22] S. Romanazzo, T. G. Molley, S. Nemec, K. Lin, R. Sheikh, J. J. Gooding, B. Wan, Q. Li, K. A. Kilian, I. Roohani, *Adv. Funct. Mater.* **2021**, *31*, 2008216.
[23] C. B. Highley, K. H. Song, A. C. Daly, J. A. Burdick, *Adv. Sci.* **2019**, *6*, 1801076.
[24] M. Shin, K. H. Song, J. C. Burrell, D. K. Cullen, J. A. Burdick, *Adv. Sci.* **2019**, *6*, 1901229.
[25] Q. Feng, D. Li, Q. Li, X. Cao, H. Dong, *Bioact. Mater.* **2022**, *9*, 105.
[26] D. J. Richards, R. C. Coyle, Y. Tan, J. Jia, K. Wong, K. Toomer, D. R. Menick, Y. Mei, *Biomaterials* **2017**, *142*, 112.
[27] L. Drakhlis, S. Biswanath, C. Farr, V. Lupanow, J. Teske, K. Ritzenhoff, A. Franke, F. Manstein, E. Bolesani, H. Kempf, S. Liebscher, K. Schenke-Layland, J. Hegermann, L. Nolte, H. Meyer, J. de la Roche, S. Thiemann, C. Wahl-Schott, U. Martin, R. Zweigerdt, *Nat. Biotechnol.* **2021**, *39*, 737.
[28] J. A. Brassard, M. Nikolaev, T. Hübscher, M. Hofer, M. P. Lutolf, *Nat. Mater.* **2021**, *20*, 22.
[29] J. N. Ferreira, R. Hasan, G. Urkasemsin, K. K. Ng, C. Adine, S. Muthumariappan, G. R. Souza, *J. Tissue Eng. Regener. Med.* **2019**, *13*, 495.
[30] A. Sheikhi, J. de Rutte, R. Haghniaz, O. Akouissi, A. Sohrabi, D. Di Carlo, A. Khademhosseini, *Biomaterials* **2019**, *192*, 560.
[31] S. Xin, K. A. Deo, J. Dai, N. K. R. Pandian, D. Chimene, R. M. Moebius, A. Jain, A. Han, A. K. Gaharwar, D. L. Alge, *Sci. Adv.* **2021**, *7*, k3087.
[32] S. V. Murphy, P. De Coppi, A. Atala, *Nat. Biomed. Eng.* **2020**, *4*, 370.
[33] Y. Fang, L. Ouyang, T. Zhang, C. Wang, B. Lu, W. Sun, *Adv. Healthcare Mater.* **2020**, *9*, 2000782.
[34] C. Li, G. C. Lau, H. Yuan, A. Aggarwal, V. L. Dominguez, S. Liu, H. Sai, L. C. Palmer, N. A. Sather, T. J. Pearson, D. E. Freedman, P. K. Amiri, M. O. de la Cruz, S. I. Stupp, *Sci. Rob.* **2020**, *5*, b9822.
[35] C. Cvetkovic, R. Raman, V. Chan, B. J. Williams, M. Tolish, P. Bajaj, M. S. Sakar, H. H. Asada, M. T. A. Saif, R. Bashir, *Proc. Natl. Acad. Sci. U. S. A.* **2014**, *111*, 10125.
[36] Y. Sun, Y. You, W. Jiang, B. Wang, Q. Wu, K. Dai, *Sci. Adv.* **2020**, *6*, y1422.
[37] H. Xuan, H. Hu, C. Geng, J. Song, Y. Shen, D. Lei, Q. Guan, S. Zhao, Z. You, *Acta Biomater.* **2020**, *105*, 97.
[38] S. M. Full, C. Delman, J. M. Gluck, R. Abdmaulen, R. J. Shemin, S. Heydarkhan-Hagvall, *J. Biomed. Mater. Res., Part B* **2015**, *103*, 39.
[39] L. Gao, M. U. Akhtar, F. Yang, S. Ahmad, J. He, Q. Lian, W. Cheng, J. Zhang, D. Li, *Acta Biomater.* **2021**, *121*, 29.
[40] Z. Tu, W. Liu, J. Wang, X. Qiu, J. Huang, J. Li, H. Lou, *Nat. Commun.* **2021**, *12*, 2916.
[41] S. P. Paşca, *Nature* **2018**, *553*, 437.
[42] C. Yu, X. Ma, W. Zhu, P. Wang, K. L. Miller, J. Stupin, A. Koroleva-Maharajh, A. Hairabedian, S. Chen, *Biomaterials* **2019**, *194*, 1.
[43] D. D. Huang, S. B. Gibeley, C. Xu, Y. Xiao, O. Celik, H. N. Ginsberg, K. W. Leong, *Adv. Funct. Mater.* **2020**, *30*, 1909553.
[44] X. Ma, X. Qu, W. Zhu, Y. Li, S. Yuan, H. Zhang, J. Liu, P. Wang, C. S. E. Lai, F. Zanella, G. Feng, F. Sheikh, S. Chien, S. Chen, *Proc. Natl. Acad. Sci. U. S. A.* **2016**, *113*, 2206.
[45] W. Ochiai, A. Hirose, T. Kawamura, K. Komachi, Y. Yamamoto, S. Kitaoka, J. Hatogai, Y. Kusunoki, R. Kon, N. Ikarashi, K. Sugiyama, *Biol. Pharm. Bull.* **2016**, *39*, 2015.
[46] P. Manikandan, S. Nagini, *Curr. Drug Targets* **2018**, *19*, 38.
[47] D. B. Kolesky, R. L. Truby, A. S. Gladman, T. A. Busbee, K. A. Homan, J. A. Lewis, *Adv. Mater.* **2014**, *26*, 3124.
[48] L. Shao, Q. Gao, C. Xie, J. Fu, M. Xiang, Y. He, *Biofabrication* **2020**, *12*, 035014.
[49] C. Colosi, S. R. Shin, V. Manoharan, S. Massa, M. Costantini, A. Barbetta, M. R. Dokmeci, M. Dentini, A. Khademhosseini, *Adv. Mater.* **2016**, *28*, 677.
[50] A. K. Miri, D. Nieto, L. Iglesias, H. H. Goodarzi, S. Maharjan, G. U. Ruiz-Esparza, P. Khoshakhlagh, A. Manbachi, M. R. Dokmeci, S. Chen, S. R. Shin, Y. S. Zhang, A. Khademhosseini, *Adv. Mater.* **2018**, *30*, 1800242.
[51] X. Zhao, S. Liu, L. Yildirimer, H. Zhao, R. Ding, H. Wang, W. Cui, D. Weitz, *Adv. Funct. Mater.* **2016**, *26*, 2809.
[52] Y. Fang, T. Zhang, Y. Song, W. Sun, *Biomed. Mater.* **2020**, *15*, 045003.